Atmospheric Predictability: Why Butterflies Are Not of Practical Importance

DALE R. DURRAN AND MARK GINGRICH

Department of Atmospheric Sciences, University of Washington, Seattle, Washington

(Manuscript received 8 January 2014, in final form 26 February 2014)

ABSTRACT

The spectral turbulence model of Lorenz, as modified for surface quasigeostrophic dynamics by Rotunno and Snyder, is further modified to more smoothly approach nonlinear saturation. This model is used to investigate error growth starting from different distributions of the initial error. Consistent with an often overlooked finding by Lorenz, the loss of predictability generated by initial errors of small but fixed absolute magnitude is essentially independent of their spatial scale when the background saturation kinetic energy spectrum is proportional to the $-5/3$ power of the wavenumber. Thus, because the background kinetic energy increases with scale, very small relative errors at long wavelengths have similar impacts on perturbation error growth as large relative errors at short wavelengths. To the extent that this model applies to practical meteorological forecasts, the influence of initial perturbations generated by butterflies would be swamped by unavoidable tiny relative errors in the large scales.

The rough applicability of the authors' modified spectral turbulence model to the atmosphere over scales ranging between 10 and 1000 km is supported by the good estimate that it provides for the ensemble error growth in state-of-the-art ensemble mesoscale model simulations of two winter storms. The initial-error spectrum for the ensemble perturbations in these cases has maximum power at the longest wavelengths. The dominance of large-scale errors in the ensemble suggests that mesoscale weather forecasts may often be limited by errors arising from the large scales instead of being produced solely through an upscale cascade from the smallest scales.

1. Introduction

In a seminal paper, Lorenz (1969, hereafter L69) showed that limits to the predictability of atmospheric circulations can arise from unobservable small-scale motions. Subsequent investigations using more sophisticated turbulence models (Leith 1971; Leith and Kraichnan 1972; Métais and Lesieur 1986) confirmed that the rapid upscale cascade of small-scale initial error imposes finite limits on the predictability of turbulent flows whose kinetic energy spectrum is proportional to the $-5/3$ power of the horizontal wavenumber k. The loss of predictability in numerical weather forecasts has, therefore, often been attributed to the upscale growth of small unresolved perturbations, particularly in forecasts of atmospheric motions at scales less than about 400 km where observations show the atmospheric kinetic energy spectrum follows a $k^{-5/3}$ power law.

As horizontal wavelengths increase beyond 400 km, the atmospheric kinetic energy spectrum gradually shifts from a $k^{-5/3}$ to a k^{-3} power law (see Fig. 5). Evidence from turbulence theory and from simulations of atmospheric flows suggests that upscale error growth is less rapid and less important in the longer-wavelength k^{-3} regime. In particular, Tribbia and Baumhefner (2004) found that the role of small-scale errors is primarily to perturb the baroclinically unstable scales, which then grow rapidly and dominate the loss of large-scale predictability. Nevertheless, upscale error propagation through the mesoscale, with its $k^{-5/3}$ spectrum, likely remains the key factor perturbing the baroclinically unstable scales and ultimately producing the loss of predictability at large scales. Our focus in the remainder of this paper will therefore be on the propagation of initial-condition errors through the mesoscale (i.e., on mesoscale predictability).

Although they only roughly approximate the dynamics of the true atmosphere, the calculations in L69 suggest that errors at wavelengths between 100 m and 1 km may destroy the predictability of motions with scales on the order of 10 km in just a few hours. Yet mesoscale numerical weather prediction models are

Corresponding author address: Dale Durran, Dept. of Atmospheric Sciences, University of Washington, Box 351640, Seattle, WA 98195.
E-mail: drdee@uw.edu

DOI: 10.1175/JAS-D-14-0007.1

now routinely used to generate 48-h forecasts that include features on scales $O(10)$ km. The justification for these attempts to forecast small-scale features at such long lead times is largely based on the proposition of Anthes et al. (1985) that phenomena generated by the interaction of the large-scale flow with known small-scale forcing (such as topography) or through the dynamics of the large-scale flow itself (such as fronts) inherit the extended predictability of the large-scale flow. According to this viewpoint, the large scale can improve mesoscale predictability by providing initial conditions capable of correctly generating uninitialized small-scale features. Recent analyses of the spectral structure of initial errors in pseudo-operational mesoscale forecasts, however, suggest that the absolute errors in the larger scales exceed those in the small scales (Bei and Zhang 2007; Durran et al. 2013) and that error growth can be closer to a quasi-uniform amplification of the errors at all wavenumbers at which the error is unsaturated rather than an upscale error cascade (Mapes et al. 2008; Durran et al. 2013).

Given this evidence for the potential importance of initial errors at large scales, our first goal is to investigate the response of the L69 model and improvements thereof (Rotunno and Snyder 2008, hereafter RS08) to a range of hypothetical initial-error distributions. Our second goal is to compare the error growth in the improved Lorenz model with initial conditions representative of those computed using ensemble forecasts with high-resolution mesoscale models. We conclude by assessing the likely practical importance of large- and small-scale errors in the context of the improved Lorenz model.

2. Initial-error growth in an improved turbulence model

The original L69 model uses the two-dimensional barotropic vorticity equation (2DV) to represent homogeneous isotropic turbulence. Lorenz also assumed that the saturation kinetic energy spectrum for the turbulence described by his model follows a $k^{-5/3}$ power law, whereas the actual saturation kinetic energy spectrum generated by two-dimensional barotropic motions varies in proportion to k^{-3}. This inconsistency was removed in subsequent studies with more sophisticated turbulence models (Leith 1971; Leith and Kraichnan 1972; Métais and Lesieur 1986) and more recently by RS08 through an elegant modification of the underlying dynamics in Lorenz's model. RS08 extended Lorenz's analysis to describe homogeneous isotropic turbulence governed by surface quasigeostrophic theory (SQG), which does generate a saturation kinetic energy spectrum following a $k^{-5/3}$ power law (Held et al. 1995).

Comparing their more consistent SQG model with Lorenz's barotropic formulation, RS08 concluded that "the basic-state spectrum is the determining factor in the error-energy evolution with the dynamical model (SQG or 2DV) playing a secondary role." The similarity of the upscale error growth in L69 and RS08 for the case of a $k^{-5/3}$ saturation kinetic energy spectrum is illustrated in Fig. 1, which shows the evolution of the error-energy spectrum at nondimensional times in the interval $0 \le t \le 1$. Figure 1a is essentially identical to Fig. 1a of RS08 and will serve as the departure point for our subsequent analysis. We believe Fig. 1b provides the first presentation of the same case from the well-known L69 model in a quantitative graphical format. In both the SQG and barotropic models, the error expands upscale as progressively longer wavelengths become saturated, with somewhat faster upscale propagation in the barotropic case. The errors remain small in those scales that are not yet saturated, although there is more error at a given unsaturated wavenumber in the barotropic case than in SQG model.

Before proceeding with further analysis, we make an additional simple improvement to the models used in L69 and RS08. The evolution of the error in L69 and RS08 is governed by the second-order ordinary differential equation

$$\frac{d^2 Z_k}{dt^2} = \sum_{l=1}^{n} C_{k,l} Z_l, \tag{1}$$

in which $\mathbf{C}$ is a constant matrix determining the interactions between various length scales, n is the total number of spectral bands, and Z_k is the ensemble mean of the kinetic energy of the perturbations KE′ about the ensemble velocity field, integrated with respect to $\ln(k)$ over the spectral band at two-dimensional horizontal wavenumber k. In the following, we refer to Z_k/k as the KE′ spectral density, or simply the "error" ($\mathrm{m^3\,s^{-2}}$).

The derivation of (1) is complex and covered thoroughly in L69 and RS08, who show that

$$C_{k,l} = \sum_{m=1}^{n} B_{k-m,l-m} N_m^2 X_m, \tag{2}$$

where N_m is the nondimensional wavenumber of the mth spectral band, X_m is the saturation kinetic energy integrated over the spectral band at wavenumber N_m, and $B_{k,l}$ is determined by the triad interactions involving wavenumbers in spectral band l that produce forcing in spectral band k. The influence of the slope of the saturation kinetic energy spectrum on error growth appears in (2) through the factor X_m, whereas the factor $B_{k,l}$

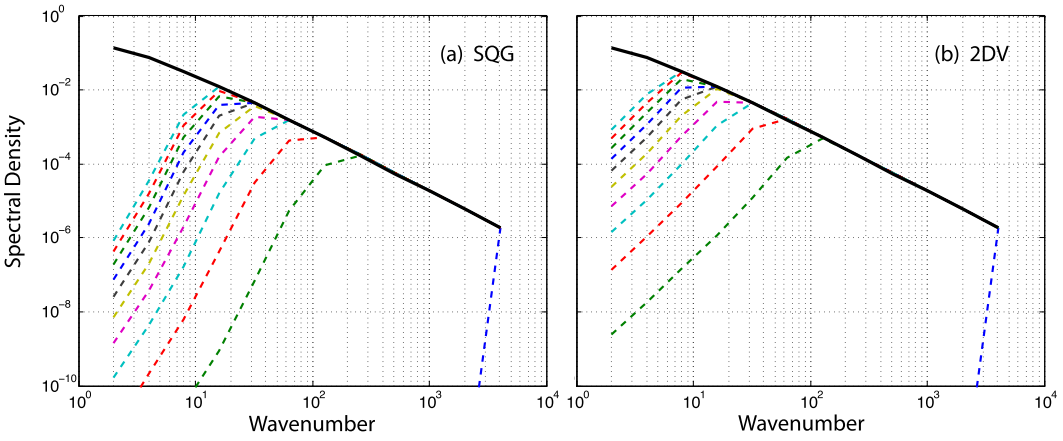

FIG. 1. Perturbation kinetic energy spectral density as a function of wavenumber k at nondimensional times $t = 0$, 0.1, . . . , 1.0 for (a) surface quasigeostrophic dynamics and (b) the barotropic vorticity equation. Following RS08, these calculations are performed using 12 modes with $\rho = 2$ and linear growth rates until saturation.

carries the direct influence of the dynamical formulation (SQG or 2DV).[1]

Nonlinearity is included in the L69 and RS08 models by abruptly cutting off the growth of Z_k when it achieves saturation by enforcing the inequality

$$Z_k(t) \le X_k. \tag{3}$$

This treatment of nonlinear saturation does not correctly capture the gradual decrease in the growth rate of Z_k that must occur as it approaches saturation. Therefore, we impose a simple nonlinear feedback that forces Z_k to smoothly asymptote to X_k. One may replace the system of n second-order differential equations shown in (1) by the equivalent system of $2n$ first-order differential equations

$$\frac{dY_k}{dt} = \sum_{l=1}^{n} C_{k,l} Z_l, \quad \frac{dZ_k}{dt} = \left(\frac{X_k}{X_k}\right) Y_k. \tag{4}$$

Perhaps the simplest nonlinear feedback that can be added to force the time tendencies of the Z_k smoothly to zero as they approach their saturation thresholds X_k is given by

$$\frac{dY_k}{dt} = \sum_{l=1}^{n} C_{k,l} Z_l, \quad \frac{dZ_k}{dt} = \left(\frac{X_k - Z_k}{X_k}\right) Y_k. \tag{5}$$

Except for the arbitrary treatment of nonlinear saturation, the derivations in L69 and RS08 are based on linear dynamics, and their derivations are fully applicable to (5) because it linearizes to (1).

[1] The dynamical formulation also influences the slope of the saturation kinetic energy spectrum.

We use (5) for our subsequent analysis and will refer to this as the smooth-saturation Lorenz–Rotunno–Snyder (ssLRS) model. The evaluations of the coefficients $C_{k,l}$ and the numerical integration of (3) were performed using MATLAB. Except for the cases in Fig. 1, adjacent wavenumbers in our truncation differ by a factor of $\rho = \sqrt{2}$, which is twice the spectral resolution used in L69 and RS08. We retain 24 wavenumbers, truncating our expansion at the same nondimensional wavenumber as RS08 (who retained 12 wavenumbers). Additional details about the numerics are given in the appendix.

Figure 2a shows the ssLRS error evolution for the same case plotted in Fig. 1a. The solution is similar to that given by RS08, but smoother because of the finer spectral resolution. Moreover, the growth slows noticeably just before the errors saturate. This delay in reaching saturation is qualitatively similar to that in the more sophisticated turbulence models shown in Fig. 6 of Leith (1971), Fig. 13 of Leith and Kraichnan (1972), and Fig. 2 of Métais and Lesieur (1986). Nevertheless, we do not wish to suggest our treatment of nonlinear saturation makes the ssLRS model the theoretical equal of these turbulence models; it simply removes an artificial discontinuity in the growth rates computed using L69 and RS08 by allowing a smooth approach to saturation.

Consider now alternative initial-error structures. Figure 2b shows an initial white-noise spectrum of sufficient amplitude to saturate the error in the smallest retained scale; similar initial states have been used in many predictability studies. The white-noise spectrum is proportional to the two-dimensional wavenumber k, so the initial errors in the longer wavelengths are very small, and as a consequence, upscale error growth via the successive saturation of larger scales is almost identical to that in Fig. 2a.

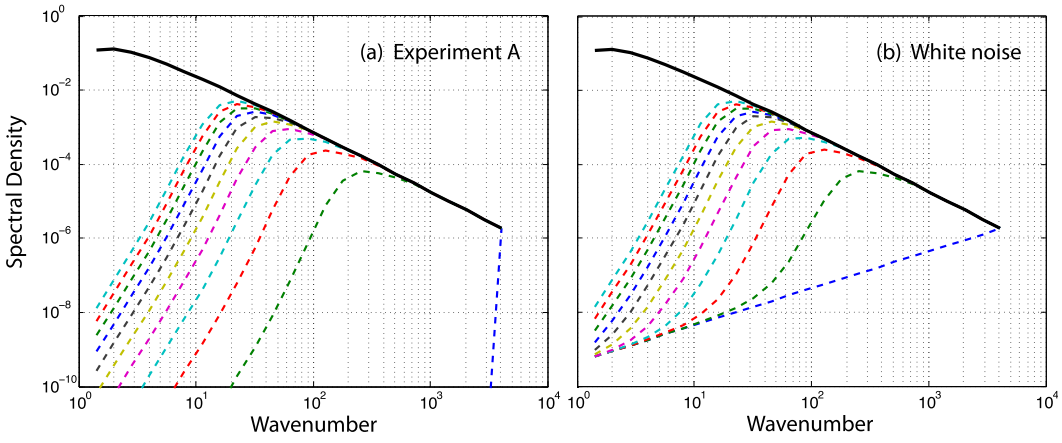

FIG. 2. KE′ spectral density Z_k/k as a function of wavenumber k at nondimensional times $t = 0, 0.1, \ldots, 1.0$ for initial error saturated at the largest wavenumber and (a) zero elsewhere and (b) following a white-noise spectrum. These and subsequent calculations are performed using 24 modes with $\rho = \sqrt{2}$ and a smooth approach to nonlinear saturation.

The error evolution for a case with all initial error at the largest scale is shown in Fig. 3a. The initial KE′ spectral density at the largest-scale $Z_1/1$ was set to X_n/n, making its magnitude identical to that placed at the smallest scale in the case shown in Fig. 2a. The upscale error growth along the saturation curve is very similar in both cases, particularly after time 0.1. Evidently, very small relative errors in the large-scale initial conditions are capable of producing upscale error propagation at rates similar to that induced by gross inaccuracies in the initial specification of the smallest scales. Further discussion of the case shown in Fig. 3a will be provided in section 4.

Another simple initial-error distribution is one with uniform relative error at all scales. Figure 3b shows growth of Z_k/k when the initial errors are 1% of the saturation KE′ spectral density X_k/k at all scales. The error growth in this situation is substantially different from those in the preceding cases. With uniform initial relative errors, the smallest scales all saturate by $t = 0.1$ and subsequent growth is largely through the amplification of the error at each unsaturated wavenumber and only secondarily upscale. Given the substantial difference in error growth between that shown in Fig. 3b and the other cases, one naturally asks what the initial-error distribution might be in actual weather forecasts. That is the focus of the next section.

3. Comparison of the ssLRS model with error growth in ensemble forecasts

a. *Growth of the KE′ spectral density in mesoscale model ensembles*

As detailed in Gingrich (2013), 100-member ensembles of two East Coast winter storms were constructed using an ensemble Kalman filter (EnKF) and integrated

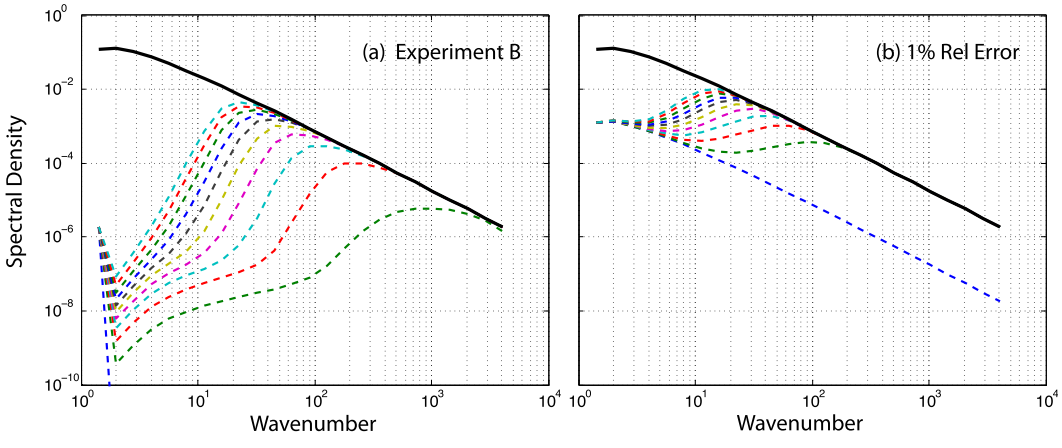

FIG. 3. As in Fig. 2, but with initial error (a) only at the largest scale and having the same magnitude as that at the smallest scale in Fig. 2a and (b) equal to $0.01X_k/k$, corresponding to a 1% relative error at all scales.

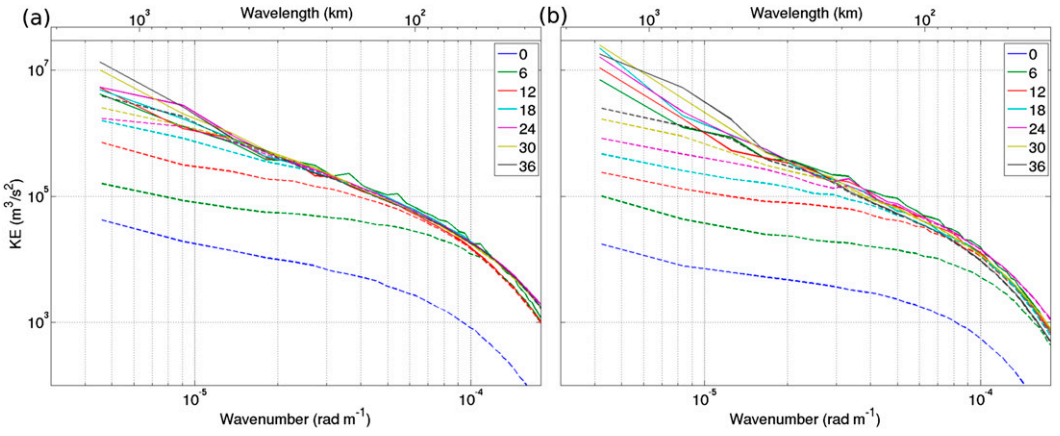

FIG. 4. Ensemble- and meridional-averaged total (solid lines) and perturbation (dashed lines) kinetic energy spectra at 500 hPa shown every 6 h (line colors given in the legend) for the COAMPS ensemble initialized (a) 1200 UTC 4 Feb and (b) 1200 UTC 25 Dec 2010. Only those wavelengths greater than $7\Delta x$ are shown; the spectrum for the initial $\widehat{\mathrm{KE}}$ is omitted.

for 36-h forecasts with the U.S. Navy's Coupled Ocean–Atmosphere Mesoscale Prediction System (COAMPS) (Hodur 1997). In these simulations, the innermost nest was convection permitting with a horizontal resolution of 5 km. The spectral density of the total kinetic energy $\widehat{\mathrm{KE}}$ was computed on the 5-km grid in the same manner as Durran et al. (2013), and similar to that of Skamarock (2004), but without time and vertical averaging.

At a given vertical level, let $u_{i,j,m}$ and $v_{i,j,m}$ denote the zonal and meridional velocities at horizontal mesh point (i, j) for ensemble member m. To avoid the influences of the nested grid boundaries, the outermost 10 grid points on each side of the nest were excluded in all calculations. Following Errico (1985), the linear trend defined by the two endpoints of the velocity fields across each east–west line of grid cells was removed for each j and m. In this way, periodicity was enforced in the fields prior to their transformation to spectral space, removing spurious energy from the smallest scales [see Fig. A2 of Skamarock (2004)]. Then, the discrete Fourier transform was applied to each $u_{j,m}$ and $v_{j,m}$. Denoting the transform of a function ϕ by $\hat{\phi}$, and the complex conjugate by ϕ^*, the kinetic energy spectral density for each j and m was computed as

$$\widehat{\mathrm{KE}}_{j,m}(\tilde{k}) = \frac{\Delta x}{2N_x}[\hat{u}_{j,m}(\tilde{k})\hat{u}^*_{j,m}(\tilde{k}) + \hat{v}_{j,m}(\tilde{k})\hat{v}^*_{j,m}(\tilde{k})]. \quad (6)$$

Here $\tilde{k}$ is the (one dimensional) zonal wavenumber, $\Delta x = 5$ km is the model grid spacing, and N_x is the total number of grid points along the ith coordinate included in the transform. Then, $\widehat{\mathrm{KE}}_{j,m}(\tilde{k})$ was averaged over both j and m to give the ensemble- and meridional-averaged one-dimensional total kinetic energy spectrum $\widehat{\mathrm{KE}}(\tilde{k})$. The solid curves in Fig. 4 show $\widehat{\mathrm{KE}}(\tilde{k})$ at 500 hPa every 6 h throughout the two ensemble forecasts initialized for 1200 UTC 4 February and 1200 UTC 25 December 2010; these times are during the periods of cyclogenesis for each storm. Only those wavelengths greater than $7\Delta x$ are shown; $7\Delta x$ is the scale beyond which numerical dissipation was deemed to significantly damp perturbations in mesoscale models by Skamarock (2004). The initialized total kinetic energy spectrum is omitted.[2]

In both events, the ensemble maintained a broad spectral region between wavelengths of approximately 100–400 km in which the observed $k^{-5/3}$ slope (Nastrom and Gage 1985) was captured quite well.[3] At wavelengths greater than approximately 400 km, the spectral slope appears to steepen with increasing forecast lead time, and particularly in the 25 December case, tends toward a k^{-3} slope. On the other hand, the spectral slope in the region with wavelengths between approximately 70 and 400 km remains fairly constant.

The perturbation kinetic energy spectral density $\widehat{\mathrm{KE}}'$ is calculated in the same manner as $\widehat{\mathrm{KE}}$, except that $u_{i,j,m}$ and $v_{i,j,m}$ are replaced with $u'_{i,j,m} = u_{i,j,m} - \overline{u}_{i,j}$ and $v'_{i,j,m} = v_{i,j,m} - \overline{v}_{i,j}$, where $\overline{\phi}$ indicates the average of ϕ over all ensemble members. Figure 4 also shows the perturbation kinetic energy spectra. As apparent in Fig. 4, the initial perturbation kinetic energy spectrum is not

[2] As discussed in Gingrich (2013), more $\widehat{\mathrm{KE}}$ is initialized in the ensemble forecasts than is maintained after 6 h of integration, likely because of physical imbalances in the EnKF analysis increments producing the initial conditions.

[3] The Nastrom and Gage (1985) data are largely collected at levels between 9 and 14 km. Our simulations also show $k^{-5/3}$ energy spectra at these higher levels.

maximized at the smallest scales. Instead the EnKF data-assimilation procedure distributed the ensemble perturbations such that their energy was maximized at the largest resolved scales. Further, the error grew significantly at the largest scales in the first 6 h of the forecast, without waiting for the upscale error propagation that characterizes the error growth in Figs. 2 and 3a. The error growth in Fig. 4 is more similar to that in Fig. 3b.

b. *The dimensional ssLRS model*

To quantitatively compare the ssLRS model's error growth with that from the COAMPS ensembles, it is necessary to assign appropriate dimensional values to the ssLRS variables. L69 dimensionalized his model by defining a length scale L and a saturation kinetic energy density scale E. We follow this approach, choosing L as the wavelength of the wavenumber-1 zonal mode at 45°N, which is 28 300 km; E is chosen to make X_k/k match observations at a wavelength near the large-scale end of the portion of the atmospheric spectrum over which a $k^{-5/3}$ power law is evident. Figure 5 shows one-dimensional kinetic energy spectra computed from aircraft data collected by Nastrom and Gage (1985) as plotted by Lindborg (1999); setting E to match these data at a wavelength of 400 km gives the value $E = 2 \times 10^5\,\mathrm{m^3\,s^{-2}}$. As also apparent from the data in Fig. 5, the atmospheric KE spectrum transitions from k^{-3} at long wavelengths to $k^{-5/3}$ over a range of wavelengths centered at about 400 km; our saturation energy spectrum is therefore specified as switching from k^{-3} to $k^{-5/3}$ at a wavelength of 400 km.[4]

The initial errors in the dimensional ssLRS model were specified by setting $Z_k(0)/k$ to $0.01X_k/k$ for the small scales following the $k^{-5/3}$ spectrum and then extrapolated along that same $k^{-5/3}$ line through the longer wavelengths. This is a simple choice giving initial errors close to those in the COAMPS ensembles at the longer wavelengths, although it underestimates $Z_k(0)/k$ in the short wavelengths. As will be discussed in section 4, the initial errors in the short wavelengths are of no importance in determining the error at 6 h and beyond.

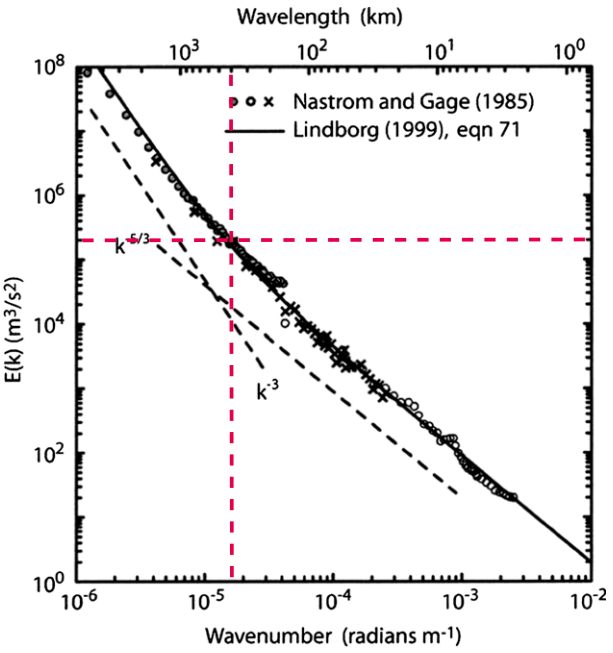

FIG. 5. Atmospheric kinetic energy density spectrum as a function of one-dimensional horizontal wavenumber adapted from Skamarock (2004), which is in turn based on data from Nastrom and Gage (1985) as plotted by Lindborg (1999). Data point used to determine the saturation kinetic energy density scale lies at the intersection of the red dashed lines.

The evolution of the KE′ spectral density in the dimensional ssLRS model and the COAMPS ensemble forecast from 1200 UTC 25 December 2010 are compared in Fig. 6. Given the extreme simplicity of the ssLRS model (only 24 degrees of freedom), the agreement with the COAMPS ensemble is surprisingly good, with relatively similar orientations and growth of the KE′ density spectra toward the saturation kinetic energy spectrum at all times $t \geq 6$ h. It should be emphasized that the time scale was not set directly, but rather is determined as $LE^{-1/2}$. The good agreement in the time evolution of Z_k/k and $\widehat{\mathrm{KE}'}$ arises from our specification of L and E, and from the dynamics underlying the ssLRS and COAMPS models.

Although the turbulence closure assumption in the ssLRS model is complex, the remaining model dynamics are quite simple, and their influence on the error growth may be assessed by comparing Fig. 7 with Fig. 6a. These four panels show the pairs of results obtained with either the SQG or barotropic vorticity equations in combination with smooth nonlinear saturation [using (5)] or with a sharp cutoff of the linear growth rate [using (3) and (4)]. While smooth nonlinear saturation does not make a dramatic difference, it does clearly slow the error growth near saturation and thereby contributes to the similarity between the KE′ spectra in the turbulence

[4] The ssLRS model expresses spectra as a function of two-dimensional horizontal wavenumber k, whereas the spectra in the COAMPS simulations (and the observations) are expressed as a function of one-dimensional wavenumber $\tilde{k}$. If the kinetic energy density spectrum follows a power law k^p for the 2D spectral wavenumber $k = (\tilde{k}^2 + \tilde{l}^2)^{1/2}$, the 1D spectrum follows the same power law $\tilde{k}^p$ for $p \leq -1$. In particular, 1D spectra differ from 2D spectral for the case $p = -5/3$ by a factor of 0.71. Scaling the ssLRS spectra so that the saturation spectrum matches the observations accounts for this constant factor.

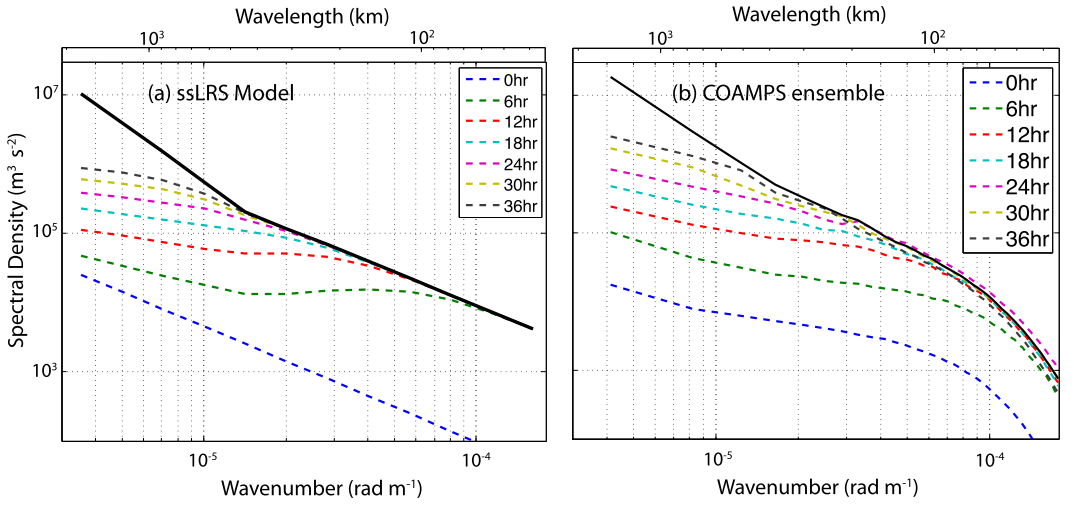

FIG. 6. (a) KE′ spectral density Z_k/k as a function of wavenumber k for the dimensional ssLRS model every 6 h (line colors given in the legend). Black curve shows the saturation spectrum X_k/k. (b) Identical to Fig. 4b, except that the curves for the total kinetic energy spectral density at each individual time are replaced by their average over hours 12–36 and plotted as the thick black line.

models and the COAMPS ensembles. Replacing SQG dynamics by the original L69 2D barotropic vorticity equation has only a modest impact, except that the errors in the largest wavelengths do grow more rapidly with barotropic vorticity dynamics. As already noted, one additional factor that can dramatically influence the error growth is the initial-error distribution, and that will be the topic of the next section.

4. Why butterflies do not matter

Adding or subtracting initial errors from selected scales is computationally quite expensive when working with large ensembles such as those that generated the data for Fig. 5, but it is trivial in the ssLRS model. Figure 8a shows the effect of removing all initial error from scales smaller than 400 km in the preceding ssLRS simulation. From hour 6 onward, there is virtually no difference between the errors shown in Fig. 8a and the case shown in Fig. 6a, which has initial errors in all scales. Data from the complimentary experiment in which all initial error is removed from the scales larger than 400 km, while the small-scale errors remain unchanged, is plotted in Fig. 8b; the error growth is clearly much slower than that shown in Fig. 8a. For example, consider the errors at $k_c = 6 \times 10^{-5}\,\mathrm{m}^{-1}$ (a wavelength of about 100 km). When initial errors are only present at wavelengths greater than 400 km (Fig. 8a), $Z(k_c)$ grows to about $X(k_c)/3$ in 6 h, but it takes about 3 times as long for $Z(k_c)$ to reach the same value

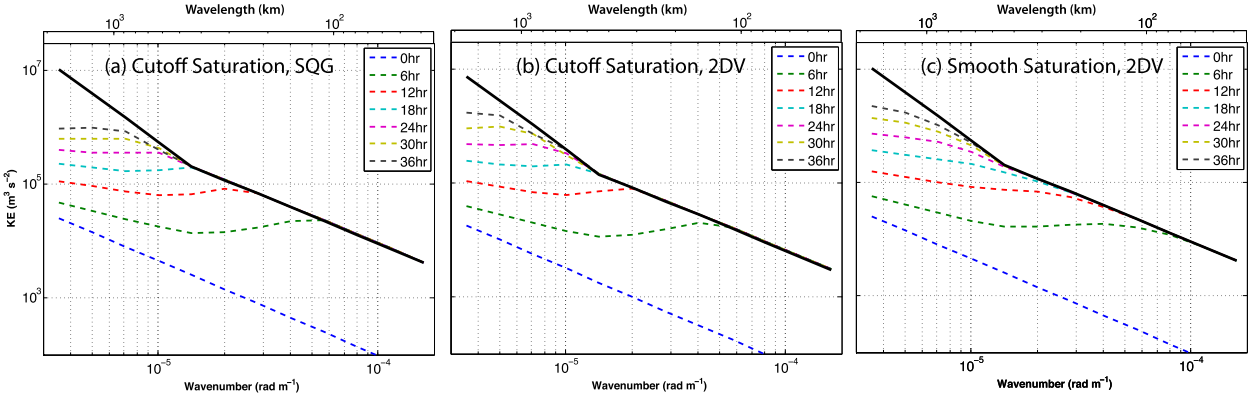

FIG. 7. As in Fig. 6a, except (a) smooth nonlinear saturation is not used, (b) surface quasigeostrophic dynamics are replaced by the barotropic vorticity equation and smooth nonlinear saturation is not used, and (c) surface quasigeostrophic dynamics are replaced by the barotropic vorticity equation.

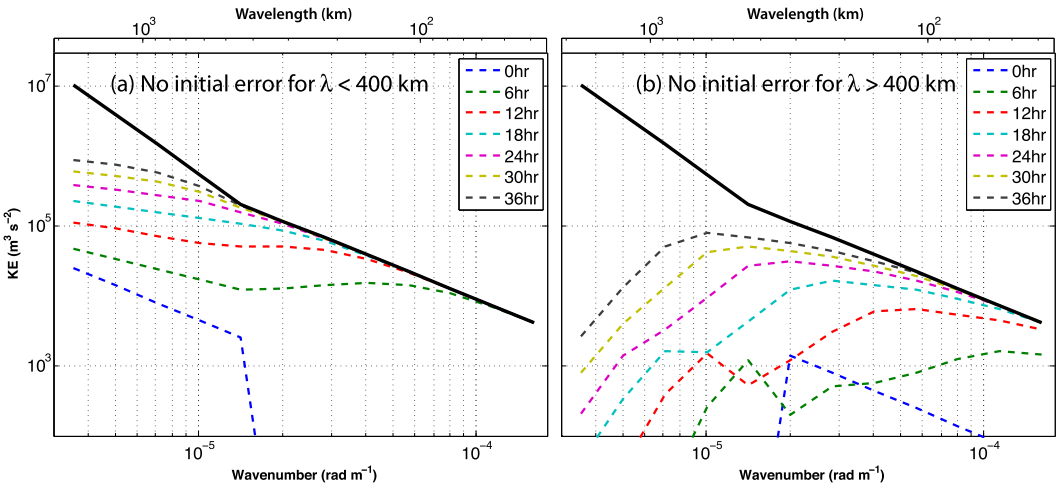

FIG. 8. As in Fig. 6a, except the initial error is removed at wavelengths (a) less than 400 km and (b) greater than 400 km.

when the errors are initially confined to scales less than 400 km (Fig. 8b).

The initial errors in $Z_k(0)$ in the case shown in Fig. 8b were 1% of their saturation value. An additional experiment was performed in which all initial error was zero, except at the smallest (6.9 km) scale, at which the error was saturated. The error growth in that case (not shown) is very similar to that plotted in Fig. 8b. This experiment, together with the cases discussed in connection with Fig. 8, imply that initial small-scale errors, including those at length scales far larger than the size of butterflies, do not matter when minor relative errors are present in the largest scales. The basic explanation for the difference between the cases in Figs. 8a and 8b is that downscale error propagation in turbulence with $k^{-5/3}$ saturation KE spectra is very fast. As discussed in both L69 and RS08 (see p. 1073), this can be appreciated by examining the structure of $C_{k,l}$ given in the appendix (Tables A1 and A2), which are for the case $n = 12$ and truncated at wavenumber 9 for brevity. The coefficients above the diagonal give the rate at which error growth at a given wavenumber is ''accelerated'' by errors at larger wavenumbers (shorter wavelengths). Conversely, the coefficients below the diagonal show the ''accelerations'' owing to the presence of errors at smaller wavenumbers (longer wavelengths). The values below the diagonal are much larger than those above, implying that downscale error propagation is much more rapid than upscale propagation.

An illustration of the relative unimportance of small-scale error was actually included in L69 but seems to have been largely overlooked, both in the conclusions of L69 and in most subsequent research. In Lorenz's famous experiment A, initial error was placed only at the shortest retained wavelength.[5] In his less well-known experiment B, the same absolute initial error was placed at the longest retained wavelength. Lorenz found that predictability was lost just as rapidly in both experiments and commented ''Evidently, when the initial error is small enough, its spectrum has little effect upon the range of predictability.''

Experiment B was repeated using the ssLRS model with smooth nonlinear saturation; the result was previously presented in Fig. 3a and may be compared to the case with identical initial absolute error at the smallest scale (experiment A), whose results are plotted in Fig. 2a. By a nondimensional time of 0.2, the initial large-scale error in experiment B has spread rapidly down scale and saturated all wavenumbers greater than a nondimensional value of approximately 400. The small-scale errors at this same time are similar, although slightly larger in experiment A, where the error at time 0.2 is saturated at all wavenumbers greater than 300. Downscale propagation rapidly spreads the initial error in experiment B to smaller scales, which quickly saturate and trigger an upscale energy cascade. This process is further illustrated in Fig. 9, which compares the evolution of the error in experiments A and B at early nondimensional times $0 \leq t \leq 0.2$.

As mentioned in connection with Fig. 1 and emphasized in RS08, the slope of the saturation KE spectrum [specified via X_m in (2)] is the key factor determining the

[5] Actually Lorenz placed the initial error at the second-to-shortest wavelength. Because he extended his model to much smaller scales, the initial error was placed at a much shorter wavelength than those considered here.

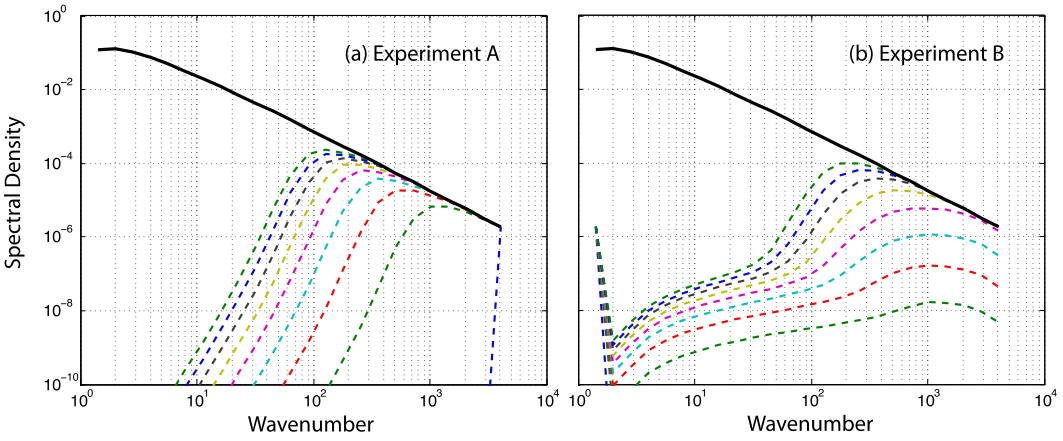

FIG. 9. As in (a) Fig. 2a (experiment A) and (b) Fig. 3a (experiment B), but for nondimensional times $t = 0, 0.025, \ldots, 0.2$.

error-energy propagation, while the direct influence of the underlying dynamics [SQG or 2DV, incorporated through $B_{k,l}$ in (2)] is secondary. This is further illustrated in Fig. 10, which shows the results of experiments A and B for systems governed by the barotropic vorticity equation with either $k^{-5/3}$ or k^{-3} spectra. Figures 10a and 10b show the results for $k^{-5/3}$, and closely approximate Lorenz's original experiments A and B.[6] The results are very similar to those shown for the ssLRS model in Fig. 2a and Fig. 3a, except that the errors grow slightly faster with 2DV dynamics. The error may grow upscale faster in the 2DV case because total energy is predominately transferred upscale by 2DV dynamics, whereas it is predominately transferred downscale by SQG dynamics (Gkioulekas and Tung 2007).

The error growth in both experiments A and B for the cases with the k^{-3} saturation KE spectra is very different from that obtained for $k^{-5/3}$. In contrast to Fig. 10a, the upscale error growth in Fig. 10c does not evolve primarily through the saturation of progressively longer wavelengths. Instead the maximum error occurs at a wavenumber $k_{\max}$ quite far from saturation (i.e., $Z_{k_{\max}}$ lies far below $X_{k_{\max}}$).[7] The influence of the slope of the saturation KE spectra is even more dramatic in experiment B. As shown in Fig. 10d, the initial errors spread downscale much more slowly than those for the $k^{-5/3}$ case, and there is no spatial scale at which the error has achieved saturation before the final nondimensional time ($t = 1$). The maximum error in Fig. 10d grows by less than a factor of 100, whereas it grows by roughly a factor of 10^4 in the cases shown in the other three panels of Fig. 10. The weak downscale error growth for the k^{-3} spectrum is associated with a very substantial reduction in the values below the diagonal of the coefficient matrix $\mathbf{C}$ relative to those for the $k^{-5/3}$ spectrum (cf. the bottom rows in Tables 1 and 3 in RS08).

Experiment B has interesting implications for researchers attempting to determine the source of initial error in forecasts of small-scale atmospheric phenomena. Even if the initial error is confined to scales at the long-wavelength end of the $k^{-5/3}$ KE spectrum (about 500 km), an individual examining errors in a case like experiment B could mistakenly conclude they originate at the smallest resolved scales because those are the scales at which the relative error first becomes nontrivial.

5. Conclusions

L69 demonstrated that the predictability of certain turbulent systems with $k^{-5/3}$ kinetic energy spectra cannot be extended beyond some finite threshold by reducing the initial-condition errors to any value greater than zero. A key factor limiting the predictability of such systems is the upscale cascade of initial errors, conceivably originating at arbitrarily small scales with arbitrarily rapid eddy turnover times. The possibility that weather forecasting may be limited by perturbations as trivial as the flapping of butterfly wings has captured the imagination of the general public.[8] Yet this focus on the possible effects of small-scale initial errors has overshadowed another equally important property

[6] Unlike L69, we continue to use smooth nonlinear saturation and higher spectral resolution with a cutoff at L69's nondimensional wavenumber 12.

[7] See also the discussion of Fig. 1b in RS08

[8] L69 actually discusses perturbations generated by a slightly larger creature: the seagull.

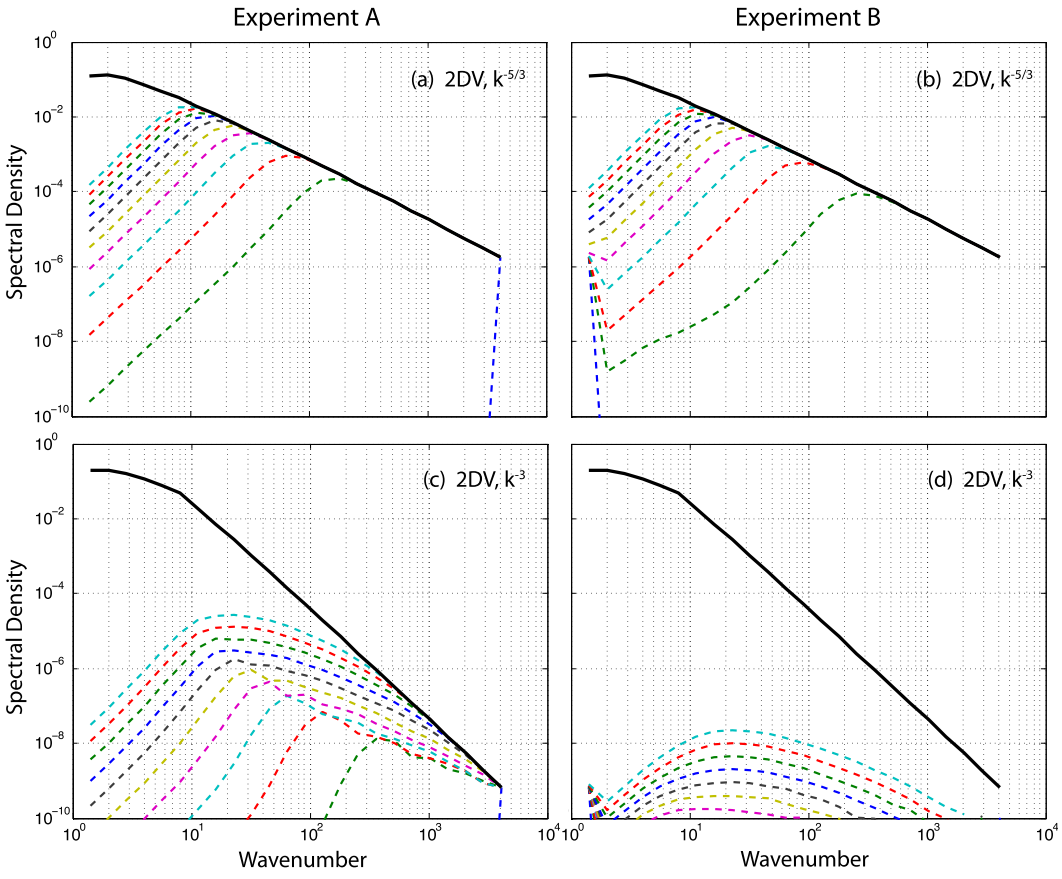

FIG. 10. As in Fig. 2a (experiment A) and Fig. 3a (experiment B), except the dynamics are for the barotropic vorticity equation. The saturation spectrum is proportional to (a),(b) $k^{-5/3}$ and (c),(d) k^{-3}.

of the L69 model—namely, the rapid downscale error propagation that also occurs in systems with $k^{-5/3}$ kinetic energy spectra. Very small initial errors in the large scales rapidly propagate downscale to the shortest retained wavelengths. The errors in the shortest wavelengths saturate, and after a brief period the subsequent upscale error growth is similar to what would have occurred if the error was limited to the smallest scales at the outset.

As evident from experiment B in L69, but largely overlooked since, a small absolute error in the KE′ spectral density produces almost the same loss in predictability no matter what its scale. Since the background saturation kinetic energy density is much bigger at longer wavelengths, very small relative errors in the large scales can have the same impact on predictability as saturated errors in the small scales. For example, consider a relative error of 100% in the KE′ spectral density at a wavelength of 10 km. Assuming a $k^{-5/3}$ spectrum, the same absolute error will produce a relative error at 400 km of $[(2\pi/10)/(2\pi/400)]^{-5/3} = 0.2\%$. Since this is a relative error in the square of the velocity times known factors, comparisons of the relative error at each scale can be applied directly to velocities. Thus, according to L69, RS08, and the ssLRS models, 0.2% errors in velocities around nominal scales of 400 km would have a similar impact on predictability as 100% errors in velocities at scales around 10 km. If one pushes the comparison well past the limits of validity of the ssLRS model and imagines that butterflies all over the world are flapping in coordination to generate a 100% relative error at a wavelength of 10 cm, a roughly equivalent impact on predictability would be exerted by a tiny 10^{-9}% relative error at a wavelength of 400 km. In any real-world event, the contributions of butterflies to uncertainties in initial conditions would be completely dwarfed by errors in the larger scales.

These estimates are of course obtained with the ssLRS model and subject to the limitations of that model. The ssLRS model is a very highly simplified representation of the actual dynamics governing atmospheric flows, and it is not as theoretically advanced as later turbulence models (Leith and Kraichnan 1972; Métais and Lesieur 1986). Nevertheless, it proved capable of estimating the

TABLE A1. Coefficients of $C_{k,l}$ for the 2DV dynamics with a $k^{-5/3}$ spectrum using $\rho = 2$ and 12 total wavenumbers. Only the coefficients for $0 \le k, l \le 9$ are shown for conciseness.

k	1	2	3	4	5	6	7	8	9
1	0.20	0.26	0.07	0.02	0.00	0.00	0.00	0.00	0.00
2	2.86	0.45	1.80	0.23	0.05	0.01	0.00	0.00	0.00
3	13.38	10.22	−1.10	8.73	0.68	0.13	0.02	0.00	0.00
4	44.9	41.5	33.1	−12.6	34.1	1.9	0.4	0.1	0.0
5	133.0	130.4	120.2	101.3	−61.9	117.8	5.3	1.0	0.2
6	372.5	370.5	363.1	334.2	298.1	−237.7	375.1	14.2	2.6
7	1010	1010	1004	984	904	851	−805	1131	37
8	2688	2687	2686	2671	2616	2404	2373	−2528	3280
9	7055	7059	7055	7053	7013	6867	6307	6494	−7542

evolution of the ensemble error growth in simulations of two East Coast snow storms with surprising fidelity (see Fig. 6). A key step required to obtain these good estimates was to initialize the ssLRS model with an error spectrum whose amplitude increased with increasing wavelength in agreement with the initial perturbation kinetic energy spectra in the EnKF-generated COAMPS ensembles. This type of initial-error structure differs significantly from those dominated by small-scale error or white noise but is consistent with recent studies of ensembles and near-twin experiments in which all initial states were produced by actual data assimilation algorithms (Bei and Zhang 2007; Durran et al. 2013), as opposed to those generated by the addition of arbitrarily chosen perturbations.

The impact of large-scale initial errors in the COAMPS ensembles and the ssLRS model suggests a need to revisit the idea that mesoscale motions typically inherit extended predictability from the large-scale flow. Mesoscale motions are indeed generated as large-scale circulations create fronts or interact with small-scale features such as topography, but there is no guarantee that the large scales can be specified with sufficiently small relative errors to ensure the correct mesoscale response. Previous research has identified instances where very small differences in the large-scale flow rapidly produced significant differences in the mesoscale response to flow over topography (Nuss and Miller 2001; Reinecke and Durran 2009) and the position of the rain–snow line (Durran et al. 2013). More extensive use of well-calibrated ensemble forecasts may provide one way of addressing the uncertainty associated with initial errors at all scales.

The comparison of the ssLRS model with the COAMPS ensembles was limited to scales ranging between 40 and 1000 km by the extent and numerical resolution of the COAMPS inner nest. This could well be the range of scales over which the ssLRS model most closely matches the atmosphere. The surface quasi-geostrophic dynamics, on which the ssLRS model is based, do not include baroclinic instability, which is a key factor in large-scale error growth (Tribbia and Baumhefner 2004; Hakim 2005). The ssLRS model is also unable to correctly describe the dynamics of convective clouds, which have relatively limited predictability (Hohenegger and Schär 2007; Weisman et al. 2008) and dominate the dynamics of small-scale atmospheric motions in many important regions of the globe. The ssLRS model describes motions that are horizontally isotropic and homogeneous, and neither of these assumptions holds in the atmosphere. Nevertheless, its ability to reasonably approximate the error growth in ensemble forecasts generated by a state-of-the-art mesoscale model does offer a measure of empirical validity for the ssLRS model and for similar

TABLE A2. As in Table A1, but for SQG dynamics.

k	1	2	3	4	5	6	7	8	9
1	0.11	0.02	0.00	0.00	0.00	0.00	0.00	0.00	0.00
2	1.18	0.18	0.30	0.01	0.00	0.00	0.00	0.00	0.00
3	8.49	4.34	−1.10	2.16	0.02	0.00	0.00	0.00	0.00
4	35.59	26.43	14.77	−9.78	10.84	0.05	0.00	0.00	0.00
5	118.1	103.4	76.7	47.8	−47.9	44.3	0.15	0.01	0.00
6	350.8	329.0	287.8	213.3	148.4	−187.0	158.9	0.40	0.02
7	980	951	892	780	578	443	−646	523	1.07
8	2648	2607	2530	2372	2075	1536	1285	−2063	1619
9	7002	6952	6846	6642	6229	5448	4032	3629	−6246

spectral turbulence models that stimulated much of the early research on atmospheric predictability.

Acknowledgments. The authors benefited from insightful conversations with Rich Rotunno and Ka-Kit Tung. Rich kickstarted this research by sharing his FORTRAN code for the RS08 model with us. Alex Reinecke provided invaluable help with the COAMPS ensemble simulations. This research was supported by the Office of Naval Research Grant N00014-11-1-0331 and completed while DRD was a visiting professor at Kyoto University's Research Institute for Mathematical Sciences.

APPENDIX

Some Details of the MATLAB Model

We used MATLAB to evaluate the elements in the **C** coefficient matrix and to integrate the differential equation given in (5) governing the error evolution. The difficult part of the implementation involves the evaluation of $C_{k,l}$, and that is the focus of the following discussion. Consider two interacting modes whose two-dimensional horizontal wavenumber vectors **K** and **L** have magnitudes K and L, and let $M = |\mathbf{K} - \mathbf{L}|$. Equation (42) of L69 gives $C_{k,l}$ defined via L69's (41) as a function of the two-dimensional integral of the functions $B_1(K/M, L, M, 1)$ and $B_2(K/M, L/M, 1)$.

RS08's Fig. A1 shows contour plots of B_1 and B_2, illustrating that $B_1(S, S, 1)$ and $B_2(S, S, 1)$ both amplify rapidly as S increases. This appears to be related to a strong singularity in the integral in (28) of L69 in the limit $K \rightarrow L$, and it makes the numerical integration of $B_1(K/M, L/M, 1)$ and $B_2(K/M, L/M, 1)$ difficult when K and L are identical and large. We performed these integrations using the MATLAB function quad2d with a relative error tolerance of 2×10^{-3} and the maximum number of function evaluations limited at 1 000 000.

The resulting $C_{k,l}$ values appear in Tables A1 and A2, which may be compared with Tables 1 and 4 of RS08, respectively. These tables are for a case with 12 nondimensional wavenumbers, although for conciseness, only the first 9 are shown in Tables A1 and A2. Following L69 and RS08, there is a factor of 2 difference between adjacent wavenumbers,[A1] and the coefficient of c in L69's (52) was set to 0.702 31. The agreement with RS08 is generally very good, but not perfect (except for $C_{9,2}$ in Table A2, for which the corresponding value in RS08 may include a typo). Our results were identical to four decimal places when the maximum number of function evaluations was reduced to 50 000, but when using either 50 000 or 1 000 000 as the limit on the maximum number of function evaluations, MATLAB issued warnings that the integral failed a global error test for just the integrals with the two highest wavenumber pairs. This warning could be eliminated by relaxing the relative error tolerance to 0.01, but that also changes the entries in the tables, moving them away from agreement with RS08. During these integrations, the quad2d flag to treat singularities was set to true, and we believe the numbers given here represent the best available estimates for $C_{k,l}$, although it also appears that some minor numerical aspects of the L69 model are difficult to pin down very accurately with absolute confidence.

[A1] Except for Fig. 1, which uses 12 modes with $\rho = 2$, all other figures in this paper show calculations using 24 wavenumbers with $\rho = \sqrt{2}$.

REFERENCES

Anthes, R. A., Y. Kuo, D. P. Baumhefner, R. M. Errico, and T. W. Bettge, 1985: Prediction of mesoscale atmospheric motions. *Advances in Geophysics,* Vol. 28B, Academic Press, 159–202.

Bei, N., and F. Zhang, 2007: Impacts of initial condition errors on mesoscale predictability of heavy precipitation along the Mei-Yu front of China. *Quart. J. Roy. Meteor. Soc.,* **133,** 83–99, doi:10.1002/qj.20.

Durran, D. R., P. A. Reinecke, and J. D. Doyle, 2013: Large-scale errors and mesoscale predictability in Pacific Northwest snowstorms. *J. Atmos. Sci.,* **70,** 1470–1487, doi:10.1175/JAS-D-12-0202.1.

Errico, R. M., 1985: Spectra computed from a limited area grid. *Mon. Wea. Rev.,* **113,** 1554–1562, doi:10.1175/1520-0493(1985)113<1554:SCFALA>2.0.CO;2.

Gingrich, M., 2013: Mesoscale predictability and error growth in short range ensemble forecasts. M.S. thesis. Department of Atmospheric Sciences, University of Washington, 70 pp.

Gkioulekas, E., and K. K. Tung, 2007: A new proof on net upscale energy cascade in two-dimensional and quasi-geostrophic turbulence. *J. Fluid Mech.,* **576,** 173–180, doi:10.1017/S0022112006003934.

Hakim, G. J., 2005: Vertical structure of midlatitude analysis and forecast errors. *Mon. Wea. Rev.,* **133,** 567–578, doi:10.1175/MWR-2882.1.

Held, I. M., R. T. Pierrehumbert, S. T. Garner, and K. L. Swanson, 1995: Surface quasi-geostrophic dynamics. *J. Fluid Mech.,* **282,** 1–20, doi:10.1017/S0022112095000012.

Hodur, R. M., 1997: The Naval Research Laboratory's Coupled Ocean/Atmosphere Mesoscale Prediction System (COAMPS). *Mon. Wea. Rev.,* **125,** 1414–1430, doi:10.1175/1520-0493(1997)125<1414:TNRLSC>2.0.CO;2.

Hohenegger, C., and C. Schär, 2007: Atmospheric predictability at synoptic versus cloud-resolving scales. *Bull. Amer. Meteor. Soc.,* **88,** 1783–1793, doi:10.1175/BAMS-88-11-1783.

Leith, C., 1971: Atmospheric predictability and two-dimensional turbulence. *J. Atmos. Sci.,* **28,** 145–161, doi:10.1175/1520-0469(1971)028<0145:APATDT>2.0.CO;2.

——, and R. Kraichnan, 1972: Predictability of turbulent flows. *J. Atmos. Sci.,* **29,** 1041–1058, doi:10.1175/1520-0469(1972)029<1041:POTF>2.0.CO;2.

Lindborg, E., 1999: Can the atmospheric kinetic energy spectrum be explained by two-dimensional turbulence? *J. Fluid Mech.,* **388,** 259–288, doi:10.1017/S0022112099004851.

Lorenz, E., 1969: The predictability of a flow which possesses many scales of motion. *Tellus,* **21,** 289–307, doi:10.1111/j.2153-3490.1969.tb00444.x.

Mapes, B., S. Tulich, T. Nasuno, and M. Satoh, 2008: Predictability aspects of global aqua-planet simulations with explicit convection. *J. Meteor. Soc. Japan,* **86A,** 175–185.

Métais, O., and M. Lesieur, 1986: Statistical predictability of decaying turbulence. *J. Atmos. Sci.,* **43,** 857–870, doi:10.1175/1520-0469(1986)043<0857:SPODT>2.0.CO;2.

Nastrom, G., and K. Gage, 1985: A climatology of atmospheric wavenumber spectra of wind and temperature observed by commercial aircraft. *J. Atmos. Sci.,* **42,** 950–960, doi:10.1175/1520-0469(1985)042<0950:ACOAWS>2.0.CO;2.

Nuss, W., and D. Miller, 2001: Mesoscale predictability under various synoptic regimes. *Nonlinear Processes Geophys.,* **8,** 429–438, doi:10.5194/npg-8-429-2001.

Reinecke, P. A., and D. R. Durran, 2009: Initial-condition sensitivities and the predictability of downslope winds. *J. Atmos. Sci.,* **66,** 3401–3418, doi:10.1175/2009JAS3023.1.

Rotunno, R., and C. Snyder, 2008: A generalization of Lorenz's model for the predictability of flows with many scales of motion. *J. Atmos. Sci.,* **65,** 1063–1076, doi:10.1175/2007JAS2449.1.

Skamarock, W. C., 2004: Evaluating mesoscale NWP models using kinetic energy spectra. *Mon. Wea. Rev.,* **132,** 3019–3024, doi:10.1175/MWR2830.1.

Tribbia, J., and D. Baumhefner, 2004: Scale interactions and atmospheric predictability: An updated perspective. *Mon. Wea. Rev.,* **132,** 703–713, doi:10.1175/1520-0493(2004)132<0703:SIAAPA>2.0.CO;2.

Weisman, M., C. Davis, W. Wang, K. Manning, and J. Klemp, 2008: Experiences with 036-h explicit convective forecasts with the WRF-ARW model. *Wea. Forecasting,* **23,** 407–437, doi:10.1175/2007WAF2007005.1.